

# Millimeter-Wave Beam Scattering and Induced Broadening by Plasma Turbulence in the TCV Tokamak

O. Chellaï,<sup>1,3</sup> S. Alberti,<sup>1</sup> I. Furno,<sup>1</sup> T. Goodman,<sup>1</sup> O. Maj,<sup>2</sup> G. Merlo,<sup>4</sup> E. Poli,<sup>2</sup> P. Ricci,<sup>1</sup> F. Riva,<sup>5</sup> H. Weber,<sup>2</sup> and the TCV team<sup>1</sup>

<sup>1</sup>*Swiss Plasma Center (SPC), École Polytechnique Fédérale de Lausanne (EPFL), Lausanne, Switzerland*

<sup>2</sup>*Max Planck Institute for Plasma Physics, Garching, Germany*

<sup>3</sup>*Princeton Plasma Physics Laboratory, Princeton, New Jersey 08543, USA*

<sup>4</sup>*Institute for Fusion Studies, University of Texas at Austin, Austin, USA*

<sup>5</sup>*Istituto Ricerche Solari Locarno (IRSOL), 6605 Locarno Monti, Switzerland*

The scattering of millimeter-wave beams from electron density fluctuations and the associated beam broadening are experimentally demonstrated. Using a dedicated setup, instantaneous deflection and (de-)focusing of the beam due to density blobs on the beam path are shown to agree with full-wave simulations. The detected time-averaged wave power transmitted through the turbulent plasma is reproduced by the radiative-transfer model implemented in the WKBeam code, which predicts a  $\sim 50\%$  turbulence-induced broadening of the beam cross-section. The role of core turbulence for the considered geometry is highlighted.

In magnetic fusion devices [1–4], millimeter-wave (mmw) beams in the electron cyclotron (EC) range of frequencies are used for plasma diagnostics [5], heating and current drive [6], and to stabilize magneto-hydrodynamic instabilities like the neoclassical tearing mode (NTM) [7, 8]. Density fluctuations, associated with plasma turbulence on the path of the mmw beam, result in local fluctuations of the mmw power that can lead to difficulties in diagnostic interpretation [9] and to potential degradation of the EC current-drive efficiency [10]. EC-beam broadening associated with the scattering of mmw from plasma turbulence is predicted for ITER [11], which could hamper its NTM stabilization capabilities [1]. However, direct experimental evidence is still missing. From the theory point of view, although Maxwell’s equations coupled to the cold-plasma model would provide an adequate description of the wave propagation away from cyclotron resonances, the sheer number of degrees of freedom required for 3D full-wave simulations makes the approach impractical. Therefore, identifying the essential physics processes that contribute to the macroscopic wave-energy transport has been a long-standing issue in the field of nuclear fusion [10–15].

In this paper, we report first direct experimental measurements of mmw beam broadening and associated scattering by plasma turbulence in the Tokamak à Configuration Variable (TCV) [16]. A high-power mmw beam is launched from the top of the TCV vessel through a limited L-mode plasma. A receiving antenna attenuates and measures the mmw-beam power arriving at the bottom of the vessel [17]. This dedicated setup maximizes both the distance between the launching position and the detector as well as the path through the plasma, making the beam broadening due to plasma turbulence, and core turbulence in particular, directly measurable for the first time in a fusion device. Using Langmuir probe (LP) data, we show that filaments or blobs intercepting the mmw beam induce fluctuations

in the detected power by instantaneously deflecting and (de-)focusing the beam, in agreement with full-wave simulations, similarly to previous observations made in basic plasma physics devices [18]. Most notably, using experimentally validated GBS fluid simulations [19] of the plasma edge and GENE [20, 21] gyro-kinetic simulations of the plasma core, we compare the time-average measured mmw-power profile with the one computed using the WKBeam code [22]—a Monte-Carlo solver for the wave kinetic equation. We show that plasma turbulence is responsible for a broadening of the time-averaged beam cross-section of  $\sim 50\%$ , which can be attributed mostly to core turbulence. The successful comparison between the experiments and the WKBeam simulations provides a direct experimental test for the physics assumptions at the basis of the reduced radiative transfer model that is employed for the description of the macroscopic wave-energy transport.

## EXPERIMENTAL SETUP

A TCV elongated (elongation  $\kappa = 1.52$ ) ohmic L-mode deuterium plasma is generated with a toroidal magnetic field on axis  $B_T = 1.41$  T. The magnetic geometry is shown in Fig. 1(a). The time-averaged electron density profile from the Thomson scattering (TS) diagnostic [23] is shown as a function of the normalized flux coordinate  $\rho_\psi$  in Fig. 1(b). The central electron density is  $n_e \approx 7.3 \times 10^{19} m^{-3}$ , while  $n_e \approx 6 \times 10^{18} m^{-3}$  at the last-closed-flux surface (LCFS). Drift-waves and ballooning modes are responsible for driving turbulence at its edge [24, 25] associated with local fluctuations of the electron density and thus of the dielectric permittivity. Figure 1(c) shows the ion saturation current  $I_{\text{sat}} \propto n_e$  [26, 27] measured by the LP [28] shown in Fig. 1(a). The fluctuations of  $I_{\text{sat}}$  are associated

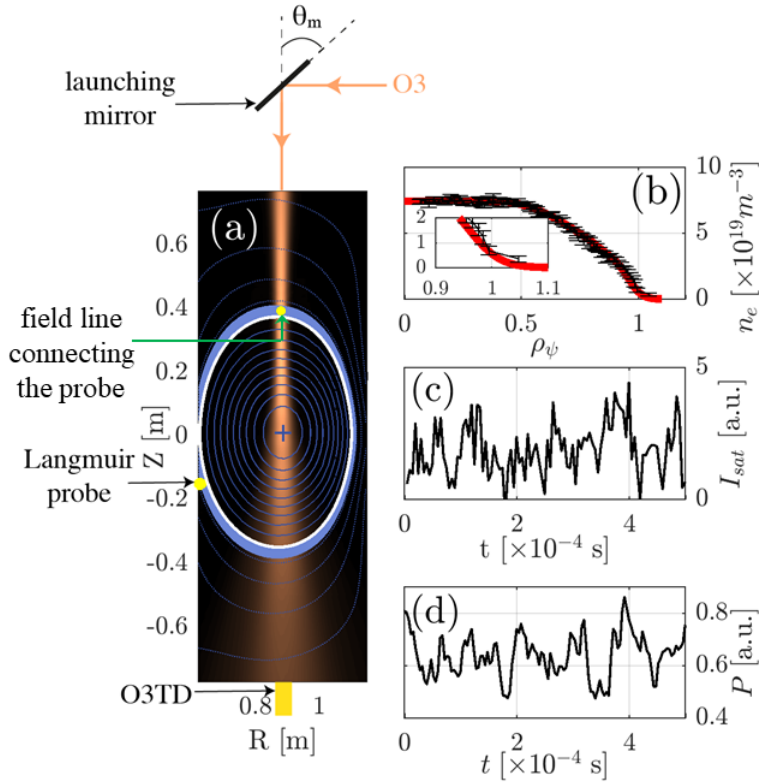


FIG. 1. (a) An O-mode mmw beam (copper-shaded area) is launched through a limited L-mode plasma, represented by its flux surfaces (contours). The blue shaded area covers the SOL region between the LCFS and the location where the density has dropped to half of its value at the LCFS. The transmitted mmw-power (d) is measured using the O3TD diagnostic. (b) Time-averaged electron density profile from the TS diagnostic and fit to the experimental data (red). The insert is a zoom of the edge region. (c) Time evolution of the ion saturation current measured at the probe location shown in (a).

with the presence of field-aligned plasma filaments at the edge of the plasma [29]. To mimic the ITER upper launcher scheme, the third harmonic EC-wave (100 kW, frequency 117.8 GHz, vacuum wavelength  $\lambda = 2.5$  mm) is launched in the ordinary mode from the top of the vessel through the plasma using a steerable focusing mirror. The beam waist ( $e$ -folding length of the  $E$ -field) in vacuum for a vertical launch of the beam is  $w = 17.60$  mm in the  $R$ -direction and is located at  $[R = 0.88 \text{ m}, Z = 0.36 \text{ m}]$ . A transmission diagnostic (O3TD)[30] was developed and installed at the location  $[R = 0.88 \text{ m}, Z = -0.77 \text{ m}]$ , displayed in Fig. 1(a) [17]. The receiving antenna is made of an  $HE_{11}$  circular waveguide (63.5 mm diameter) topped with an array of 241 circular holes (with a cut-off frequency for the lowest order  $TE_{11}$  circular mode of  $f_c = 146.4$  GHz) acting as a  $-55$  dB attenuator. The mmw-power collected by the antenna is coupled to a WR6.5 rectangular waveguide, oriented in the ordinary-mode, through a lens horn

antenna and is measured by a Schottky diode. The measured mmw-power  $P$  coupled to the O3TD antenna is shown in black in Fig. 1(d). The level of fluctuation is  $\approx 20\%$  and is partly caused by  $n_e$  changes associated with the core sawtooth activity and, as will be detailed later, by plasma turbulence.

## INSTANTANEOUS EFFECT OF BLOBS ON THE MMW BEAM

We first show that turbulent structures localized at the edge of the plasma are responsible for *instantaneous* fluctuations of the measured mmw-power.

### Verifying the field-aligned nature of the blobs in TCv

We confirm the field-aligned nature of the blobs by varying the plasma current (and thus the tilt of the magnetic field lines). Whether or not a blob detected by a Langmuir probe crosses the path of the mmw beam depends on the location of the intersection between the magnetic field line connecting the probe and the plane of the mmw beam (see Fig. 2(a)). This intersection is shown in Fig. 2(a) and can be controlled by changing the tilt of the magnetic field line and thus by varying the plasma current  $I_p$ . We investigate the influence of  $I_p$  on the maximum of the correlation function  $|C_0|_{max}$  of the detected mmw-power signal  $P(t)$  and the  $I_{sat}(t)$  signal measured by the probe shown in Fig. 1(a) and the corresponding time lag  $\delta t_{max}$  in Fig. 2(b) and (c)). The errorbars are given by the uncertainty in the estimate of  $|C_0|_{max}$  and are equal to  $\frac{1-|C_0|_{max}^2}{\sqrt{N}}$ , where  $N \sim 2000$  [31]. Figure 2(b) shows that  $|C_0|_{max}$  increases for  $I_p$  ramping from  $-278$  kA to  $-271$  kA — the intersection is moving to the center of the mmw beam — where it reaches its maximum value. The seemingly low value of 0.14 is explained by the fact that a blob detected by the Langmuir probe contributes only partly to the mmw-signal fluctuations. The value of  $|C_0|_{max}$  then decreases for  $I_p$  ramping up from  $-271$  kA to  $-260$  kA — the intersection, and thus the detected blob, is moving away from the center of the beam. For  $I_p > -260$  kA, the  $I_{sat}$  signal from the probe no longer exhibits a significant level of correlation to the  $P$  signal ( $|C_0|_{max} < 0.06$ ) and the intersection is far away from the beam path.

Figure 2(c) shows that the time lag  $\delta t_{max}$  decreases linearly, from  $\delta t_{max} = +4 \mu\text{s}$  to  $\delta t_{max} = -44 \mu\text{s}$ , when  $I_p$  increases from  $-278$  kA to  $-260$  kA. When  $\delta t_{max}$  is negative (positive), the turbulent structure affects the mmw propagation before (after) being detected by the Langmuir probe. From the values of  $\delta t_{max}(I_p)$  and the knowledge of the position of the intersection between the corresponding field line and the path of the beam, we

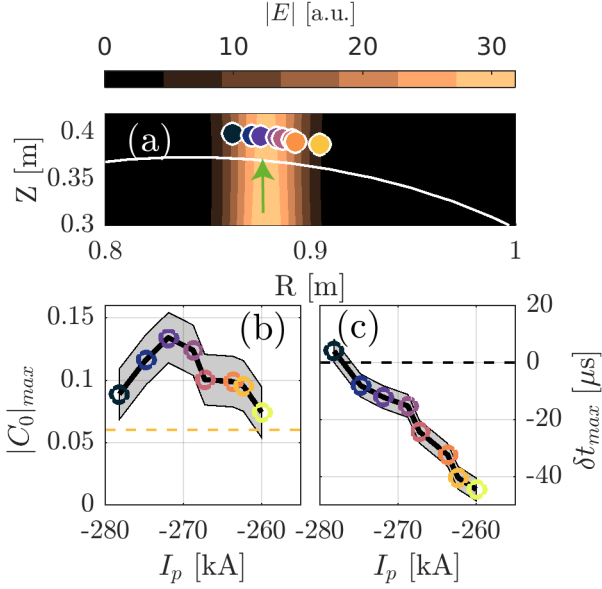


FIG. 2. Correlation between  $P$  and  $I_{sat}$ . (a) The colored circles represent the intersection of the field lines connecting the Langmuir probe and the mmw beam (the amplitude of the associated electric field amplitude is given by the copper-shaded surface) at the plasma currents shown in (b) and (c). The white line represents the last closed flux surface. (b) Maximum of the cross-correlation function between  $P$  and  $I_{sat}$  measured by the Langmuir probe as a function of the plasma current. The level  $|C_0|_{max}$  above which the correlation is considered significant is indicated by the yellow dashed line. (c) Time lag at which the maximum level of cross-correlation given in (b) occurs. The errorbars (gray area) in (a) are given by the statistical uncertainty in the estimate of  $|C_0|_{max}$  and in (b) by the sampling period of the signals.

deduce a quasi-poloidal speed  $v$  associated with the motion of the structure  $|\mathbf{v}| \approx 0.9 \text{ km} \cdot \text{s}^{-1}$  directed clockwise. This is found to be in good agreement with measurements performed with a fast-reciprocating probe [32, 33].

#### Effect of a typical blob on the mmw beam

To elucidate the effect of a typical blob on the mmw beam, we perform conditional sampling (CS) [34] on  $P$  and  $I_{sat}$  over  $N \approx 300$  blob events with a time window centered around each event. Events are defined as local maxima fulfilling the condition  $I_{sat} > \langle I_{sat} \rangle + 2\sigma$  with  $\langle I_{sat} \rangle$  and  $\sigma$  being respectively the time-averaged value and the standard deviation of  $I_{sat}$  calculated over the entire time trace. All quantities obtained with CS are labeled with a tilde, except  $\tau$  which is the time relative to the blob event,  $\tau = 0 \text{ } \mu\text{s}$  corresponding to the detection of the blob. The LP shown in Fig. 1(a) is used for blob detection. This is equivalent to detecting a blob passing by the location  $[R = 0.88 \text{ m}, Z = 0.4 \text{ m}]$  at  $\tau = 0 \text{ } \mu\text{s}$ . The result of CS of the detected mmw-power is presented in

Fig. 3(a). They show that the conditionally-sampled blob increases the mmw-power transmitted to the O3TD antenna at  $\tau = -50 \text{ } \mu\text{s}$  and decreases it at  $\tau = -14 \text{ } \mu\text{s}$ . The resulting level of fluctuation  $\delta\tilde{P}/\langle P \rangle$  is  $\sim 8\%$ .

#### Comparison with full-wave simulations

To understand the deflection of the beam due to a blob intersecting the beam path, we perform numerical simulations. Various methods are currently available for the description of wave beams in fusion plasmas [36]. However, since the typical blob size  $L_b$  is comparable to or even smaller than the beam width  $w$ , standard beam-tracing methods [35] do not apply. In our experiments, the blob size compared to the wavelength gives  $L_b/\lambda \sim 4$  which could be considered large enough for ray tracing methods [36] to apply [12], but ray tracing methods cannot account for diffraction effects [46]. Moreover in a turbulent plasma there is a finite probability to have blobs of size smaller than the average  $L_b$ , thus violating the validity conditions of ray tracing. In this case, a more recent generalization of the ray- or beam-tracing approach [10] or a full-wave model is needed. We use 2D full-wave simulations [17, 18] based on COMSOL MULTIPHYSICS [37]. The absorption being negligible in our experiments, the dielectric permittivity of the plasma is computed from the cold-plasma model and depends on  $n_e(\mathbf{x}, t)$  and  $\mathbf{B}(\mathbf{x})$  [38], where  $t$  is frozen. The equilibrium  $\langle n_e(\mathbf{x}) \rangle$  is taken from the TS data and  $\mathbf{B}(\mathbf{x})$  from the equilibrium code LIUQE. CS is applied to  $\delta n_e(\mathbf{x}, t) = n_e(\mathbf{x}, t) - \langle n_e(\mathbf{x}) \rangle$  from the GBS simulations to reconstruct the 2D evolution of  $\delta\tilde{n}_e(\mathbf{x}, t)$  associated with the blob propagation. The reference signal  $\delta n_e(\mathbf{x}_0, t)$  is used, where  $\mathbf{x}_0$  is the location of the GBS grid point in the poloidal plane corresponding to the location  $[R = 0.88 \text{ m}, Z = 0.4 \text{ m}]$  mentioned before. Two snapshots of  $\delta\tilde{n}_e$  are shown in Fig. 3(b) and (c). The conditionally-sampled blob has a typical full-width half-maximum size  $L_b \approx 1 \text{ cm}$  in the direction transverse to the magnetic field and a quasi-poloidal rotation motion with a velocity of  $|\mathbf{v}| \approx 0.92 \text{ km} \cdot \text{s}^{-1}$ , in agreement with the value of  $|\mathbf{v}| \approx 0.9 \text{ km} \cdot \text{s}^{-1}$  found previously.

As in the experiments, the numerical beam is launched vertically. The simulations are performed at 15 CS times  $\tau_i$ , with  $\delta\tau = \tau_{i+1} - \tau_i = 10 \text{ } \mu\text{s}$ . Figure 3(b) and (c) show the fluctuations of the conditionally-sampled electric field amplitude  $\delta|\tilde{\mathbf{E}}(\mathbf{x}, \tau)| = |\tilde{\mathbf{E}}(\mathbf{x}, \tau)| - \langle |\mathbf{E}(\mathbf{x})| \rangle$  of the mmw beam caused by the propagation of the blob. In Fig. 3(b),  $\delta\tilde{n}_e < 0$  preceding the blob is responsible for the focusing of the mmw beam, resulting in an increase of mmw power at the location of the O3TD diagnostic. Later (Fig. 3(c)), the blob with  $\delta\tilde{n}_e > 0$  causes a defocusing of the mmw beam behind the blob, on the receiver side, decreasing  $\delta\tilde{P}$ . These observations are in agreement with those previously made in a simple magnetized torus

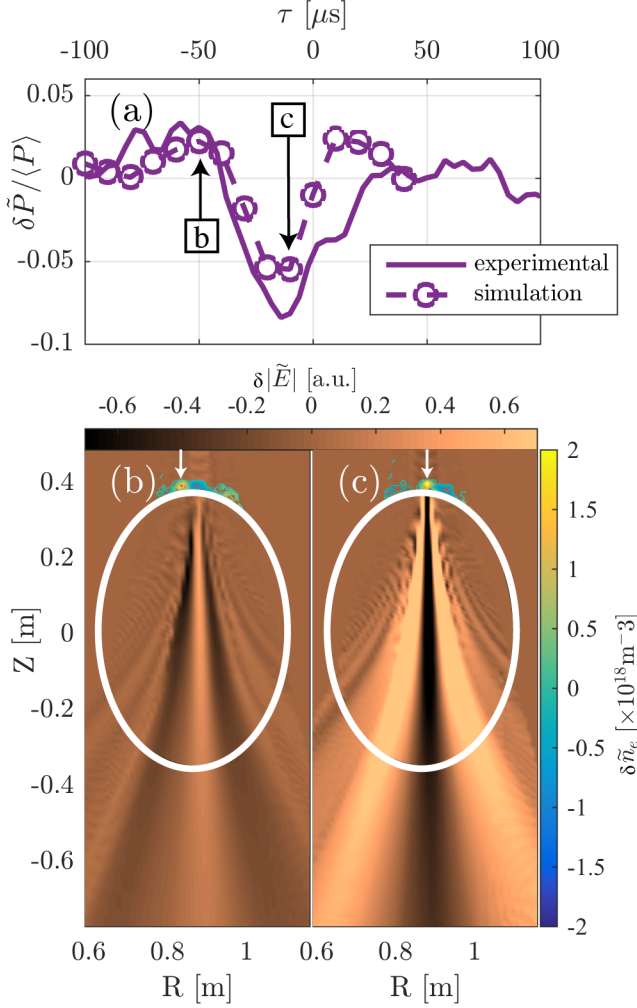


FIG. 3. (a) CS time evolution of the detected mmw-power (solid line) using the LP shown in Fig. 1(a). Experimental results (solid line) are compared to numerical simulations (dashed line). (b) and (c) Snapshots of the fluctuation of the electric field norm resulting from the propagation of the blob (indicated by the white arrow) at the times indicated in (a). The white contour is the LCFS. (b) A structure with  $\delta \tilde{n}_e < 0$  preceding the blob focuses the mmw beam. (c) The blob defocuses the mmw beam.

[18]. The resulting  $\delta \tilde{P}/\langle P \rangle$  is shown in Fig. 3(a) and is successfully compared with the experimental measurements, suggesting concomitantly a correct description of the SOL turbulence by the GBS code.

### TIME-AVERAGED EFFECT OF PLASMA TURBULENCE ON THE MMW BEAM PROFILE

We turn now to the *time-averaged* effect of plasma turbulence on the beam profile. To this goal, experiments are performed where the poloidal angle of the launch-

ing mirror is swept from  $\theta_m = 44^\circ$  to  $\theta_m = 46^\circ$ , with  $\theta_m = 45^\circ$  corresponding to the vertical launch of the beam. To ensure that the variations of  $n_e(\mathbf{x}, t)$  associated with the sawtooth oscillations do not affect the  $P(\theta_m)$  profile,  $P$  is averaged in a 0.5 ms time window occurring 1 ms after the sawtooth crash, longer than the autocorrelation time ( $\sim 10^{-5}$  s) of the turbulence. During this time interval,  $\Delta\theta_m \sim 0.001^\circ$  and  $(\Delta n_e/n_e)_{\text{sawtooth}} < 1\%$ . In Fig. 4(a),  $P(\theta_m)$  is shown and fitted by a Gaussian—in black—  $P(\theta_m) = Ae^{-2(\frac{\theta_m - \theta_0}{w_\theta})^2}$  with a width of  $w_{\theta, \text{exp}} = 0.94^\circ$ .

### WKBBeam simulations for the mmw beam propagation

The  $P(\theta_m)$  profile is compared to the one computed by the WKBBeam code [22], which was successfully benchmarked against full-wave codes [17, 39] and validated in vacuum against experiments [17]. The WKBBeam code solves a radiative transfer model for the wave energy density, accounting for refraction, diffraction, resonant damping and scattering by density fluctuations of arbitrary spatial size under the Born approximation [39, 40]. Time-dependent density fluctuations are modeled as a time-independent random density field. Time-averages of relevant physical observables are computed as ensemble-averages (ergodic hypothesis). The scattered wave is represented by a Born series truncated to the lowest order (Born approximation). Remarkably, the resulting equation for the wave-field correlation can be analyzed by means of the Wigner-Weyl transform in the short-wavelength limit, even though the fluctuations have finite probability to generate short-scale structures, since this limit is applied to the equation for the field correlation, not to the wave field directly. Similarly to the full-wave simulations, mmw beam and plasma parameters are taken from the experiments. For scattering, the WKBBeam code requires two functions of the coordinates  $(\rho_\psi, \theta)$  in the poloidal plane— $\rho_\psi$  being the normalized flux coordinate and  $\theta$  the poloidal angle with  $\theta = 0, \frac{\pi}{2}$  on the low-field side and upward vertical from the magnetic axis, respectively: the relative r.m.s. of electron density fluctuations  $\delta n_{e, \text{rms}}/\langle n_e \rangle$  and the perpendicular correlation length  $L_\perp$ , defined by  $\langle \delta n_e(\mathbf{x} + \frac{\mathbf{s}}{2}) \delta n_e(\mathbf{x} - \frac{\mathbf{s}}{2}) \rangle \propto \exp(-\frac{|\mathbf{s}_\perp|^2}{2L_\perp^2})$  where  $L_\perp$  is evaluated at the coordinates  $(\rho_\psi, \theta)$  of the point  $\mathbf{x}$  and  $\mathbf{s}_\perp = \mathbf{s} - (\mathbf{b} \cdot \mathbf{s})\mathbf{b}$ ,  $\mathbf{b} = \mathbf{B}(\mathbf{x})/B(\mathbf{x})$ . These two functions are constructed from the simulations used above based on the GBS code [41] in the SOL, and from gyro-kinetic simulations with the GENE code [21, 42] in the core. In the GBS domain defined by  $1.01 \leq \rho_\psi < 1.11$ , simulations allow us to reconstruct the values of  $\delta n_{e, \text{rms}}/\langle n_e \rangle$  on a regular grid in  $(\rho_\psi, \theta)$  which are then interpolated. In the core region,  $\rho_\psi \leq \rho_c = 0.8$ , GENE simulations give  $\delta n_{e, \text{rms}}/\langle n_e \rangle$  for three values of  $\rho_\psi$  and  $\theta = \frac{\pi}{2}$ , shown in Fig. 4(b). There-

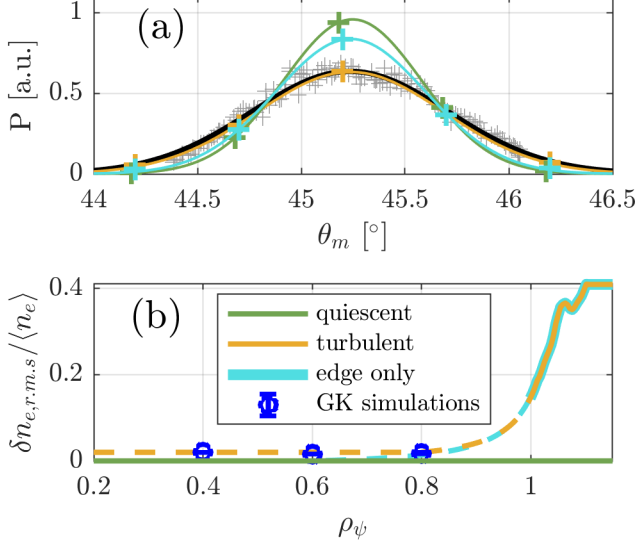


FIG. 4. (a) Comparison between the measured mmw-power (gray crosses) as a function of the injection mirror angle  $\theta_m$  and results from WKBeam simulations. The black line is a Gaussian fit to the experimental measurements. (b) Profiles of the electron density fluctuation level from the GBS simulations. The profiles are extrapolated for  $\rho_\psi < 1$  as explained in the text. Results from gyrokinetic simulations are shown in dark blue.

fore a constant value of 2% is chosen to match GENE results for  $\rho_\psi \leq \rho_c$ , and that is connected to the interpolated GBS data by means of an analytical model guided by reflectometry measurements [43, 44]. In addition, we also consider another profile, labeled “edge only”, in which  $\delta n_{e,rms}/\langle n_e \rangle = 0$  in the core so that only the edge fluctuations are accounted for. These profiles and data are shown in Fig. 4(b) for  $\theta = \frac{\pi}{2}$ . As for  $L_\perp$ , WKBeam simulations have been performed with different constant values of  $L_\perp$ , namely  $L_\perp = 0.4, 1$  and  $1.4$  cm matching the GENE estimates ( $L_\perp = 1.01, 1.39, 0.42$  cm at  $\rho_\psi = 0.4, 0.6, 0.8$ , respectively), as well as with  $L_\perp \propto \rho_s$  where  $\rho_s$  is the sound Larmor radius, which is a function of  $(\rho_\psi, \theta)$ , and the proportionality constant is fitted. For comparison we also consider a “quiescent” plasma, i.e.  $\delta n_{e,rms} = 0$ .

#### Evidence of mmw-beam broadening due to plasma turbulence

For each injection angle, WKBeam computes the power flux coupled to the O3TD antenna. The WK-Beam profiles are normalized so that the amplitude of the turbulent case matches the experimental one ( $A_{\text{turb}} = A_{\text{exp}}$ ). The profiles are shown in Fig. 4(b) for  $L_\perp = 1$  cm (which matches the GENE estimate in the core) and compared to the experimental measurements. We find that

the width of the WKBeam profile computed for the “turbulent” case ( $w_{\theta,\text{turb}} = 0.90^\circ$ ) is in good agreement with the experimental one ( $w_{\theta,\text{exp}} = 0.94^\circ$ ). The two WK-Beam profiles obtained for the “quiescent” and “edge only” cases are narrower ( $w_\theta \approx 0.66^\circ$  and  $w_\theta \approx 0.73^\circ$ , respectively) and are not in agreement with the experimental one. The difference is due to a broadening of the mmw beam associated with the scattering from plasma turbulence occurring along the path of the beam. We find that the WKBeam profile is sensitive to changes of the core value of  $\delta n_{e,rms}/\langle n_e \rangle$ , but depends weakly on  $L_\perp$ , in the considered range. The profile obtained with  $L_\perp \propto \rho_s$  is also very close to that of Fig. 4(a). Indeed, the variable  $L_\perp$  model evaluates to  $\approx 1$  cm for small  $\rho_\psi$ . These observations suggest that, in this particular setup and although the edge turbulence contributes to broadening the profile, the high density core plasma plays the major role in the broadening (cf. discussion below). Indeed, the width of the mmw beam ( $w_R = 0.24$  m)—computed at  $1/e$  in electric field—in the “turbulent” case is  $\sim 50\%$  broader than the “quiescent” ( $w_R = 0.16$  m) case and  $\sim 30\%$  broader than the “edge only” ( $w_R = 0.18$  m) case. The agreement between WKBeam predictions and the observed transmitted power supports the validity of the underlying physics assumptions—(i) the ergodic hypothesis, (ii) the Born scattering approximation, and (iii) the short-wavelength limit—within the limits set by the uncertainties on both the measurements and the density-correlation model (which has been carefully constrained by simulations and measurements). To our knowledge, this is the first direct experimental measurement of this effect for EC wave beams in tokamak plasmas.

## DISCUSSION OF THE RESULTS AND COMPARISON WITH ITER

The role of core turbulence in broadening the mmw beam in TCV seems to contradict previous ITER studies [10] which show that edge turbulence is mainly responsible for the broadening of the beam. This difference is a consequence of the different plasma parameters and propagation paths in both machines and can be understood employing an analytical expression for the beam width obtained in slab geometry [45]. The squared beam width reads

$$w^2(\tau) = w_{\text{GB}}^2(\tau) + \int_0^\tau \frac{1}{L_\perp} \sqrt{\frac{2\pi}{\varepsilon_0}} \left\langle \frac{\delta n_e^2}{n_{e,c}^2} \right\rangle (\tau - \tau')^2 d\tau', \quad (1)$$

where  $\tau$  is a parameter related to the arc-length  $\ell$  of the beam path by  $d\ell = \sqrt{\varepsilon_0} d\tau$ ,  $\varepsilon_0 = 1 - n_e/n_{e,c}$  being the O-mode cut-off density, and  $w_{\text{GB}}$  is the standard width of a Gaussian beam in slab geometry without turbulence [46]; both  $L_\perp$  and  $\langle \delta n_e^2 \rangle$  can depend on the position along the beam path. Eq. (1) has been obtained



by Sysoeva et al. [15] with different methods and it is recovered here directly from the analytical solution of the WKBeam model specialized to the case of O-mode propagation in slab geometry, thus proving that these two different theories yield the same conclusion on the beam broadening.

Eq. (1) captures the fundamental dependencies of the turbulence-induced beam broadening. To estimate the relative importance of core and edge turbulence for the beam broadening, we construct the ratio between the turbulent contributions of core and edge to the squared beam width as suggested by Eq. (1) —taking  $\langle \delta n_e^2 / n_{e,c}^2 \rangle$  as piece-wise constant and neglecting  $\sqrt{\varepsilon_0}$ . For TCV, defining the “edge” as the region  $\rho_\psi > 0.9$  where  $\delta n_{e,\text{rms}} / \langle n_e \rangle > 5\%$ , one can estimate from Fig. 4 that the “core” region is ca. 9 times broader than the “edge” region so that  $(\Delta \rho_{\text{core}} / \Delta \rho_{\text{edge}})^3 \approx 9^3$ . Moreover,  $(\delta n_{e,\text{rms}} / \langle n_e \rangle)_{\text{core}}^2 / (\delta n_{e,\text{rms}} / \langle n_e \rangle)_{\text{edge}}^2 \approx 10^{-2}$  and  $\langle n_e \rangle_{\text{core}}^2 / \langle n_e \rangle_{\text{edge}}^2 \approx 10\text{--}10^2$ , depending on where the values are taken. We find  $(10\text{--}10^2) \times 10^{-2} \times 9^3 \gg 1$ , which shows that the core has indeed a much stronger “scattering effect” than the edge. For the ITER upper launcher the result of a similar estimate would be opposite. For tearing-mode stabilization, the beam does not cross the whole plasma, but is absorbed on the outer rational surfaces. Moreover, the separatrix density in ITER is predicted to be a significant fraction of the central density, differently from the TCV profiles considered here.

As a concluding remark, we stress here that Eq. 1, while correctly capturing the scalings of the beam width with the various plasma parameters, cannot be employed for a quantitative assessment, mainly because of the simplifying assumptions on the plasma geometry [45]. For a quantitative comparison with the experiments, WKBeam simulations as described above are needed. Indeed, we can understand the applicability of the analytical results to an actual plasma equilibrium by comparing the beam width predicted by equation (1) with that computed from the full WKBeam solution in the actual TCV equilibrium. We consider the particular beam launched with mirror angle  $\theta_m = 45^\circ$  as its central trajectory suffers little refraction and remains almost vertical in the TCV vessel (the horizontal position of the central point of the beam deviates by about 1.3 cm from its launching value over the whole length of the propagation path which is about 200 cm). The numeric beam width is computed from the poloidal projection of the wave energy density at constant  $Z$ , where  $Z$  is the vertical coordinate in the laboratory frame. The evaluation of the analytical formula (1) is less straightforward since the plasma equilibrium is not a slab. In the evaluation of the integrals and in (1) we have used the values of the electron density and relative root-mean-square density fluctuations on the central ray of the beam as evaluated by WKBeam. The central ray is always traced in the

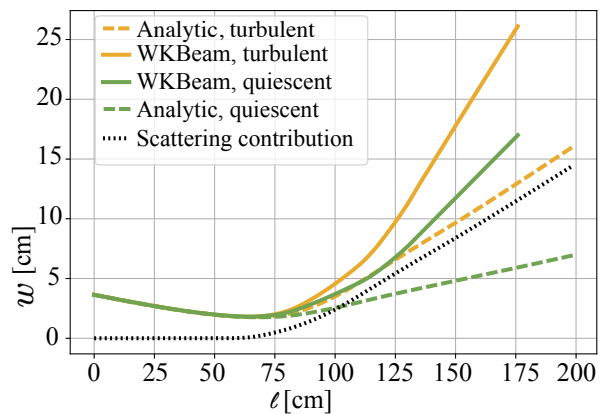


FIG. 5. Comparison of beam widths computed in the realistic TCV equilibrium with  $\theta_m = 45^\circ$ , with —model with constant  $L_\perp = 1$  cm— and without density fluctuations. The width of  $Z = \text{constant}$  sections of the beam are estimated from the poloidal projection of the wave energy density computed by WKBeam. The corresponding analytical beam width are obtained by equation (1), respectively, using the electron density and root-mean-square fluctuations on the central ray of the actual beam. The dotted line shows the analytical scattering contribution defined after equation (1).

quiet plasma equilibrium and it is not affected by density fluctuations. In this way the exact same density and fluctuations are used in the analytical formula and in WKBeam. The beam widths thus obtained are shown in figure 5. In addition, figure 5 also shows the analytic and numerical beam width for the same TCV beam but without density fluctuations. In this case we see a clear quantitative disagreement between the analytic and the numerical result, both with and without scattering on density fluctuations, although the qualitative behavior appears correct. Therefore, even though Eq. 1 captures the fundamental dependencies of the turbulence-induced beam broadening, the realistic plasma equilibrium with its non-uniform magnetic field and toroidally shaped iso-contours of the electron density is too complex for the simple slab model with the assumption of perpendicular propagation to describe quantitatively.

## CONCLUSION

In summary, we presented the first evidence of mmw scattering and turbulent broadening in a tokamak using a combination of *in-situ* measurements of the electron density and experimentally validated plasma turbulence simulations. In TCV, instantaneous deflections of the beam due to the presence of edge blobs, inducing fluctuations of the mmw power of the order of  $\sim 10\%$  have been demonstrated. Most notably, using a dedicated setup, we measured directly and for the first time a  $\sim 50\%$  turbulence-induced broadening of the time-averaged

cross-section of a beam traversing vertically the TCV plasma column. All these results agree with numerical simulations based on a combination of turbulence codes and wave-equation solvers, confirming the reliability of the theoretical approach and, in particular, the validity of the underlying physics assumptions of WKBeam. Differences between different injections scenarios (e.g. TCV and ITER) are explained on the basis of the developed model.

*The authors acknowledge useful discussions with Kate Sysoeva and the first author would like to thank S. Coda for his support on the planning of the experimental sessions on TCV. This work has been carried out within the framework of the EUROfusion Consortium and has received funding from the Euratom research and training programme 2014-2018 and 2019-2020 under grant agreement No 633053. The views and opinions expressed herein do not necessarily reflect those of the European Commission. The views and opinions expressed herein do not necessarily reflect those of the European Commission. This work was supported in part by the Swiss National Science Foundation.*

- 
- [1] E. Poli *et al.*, Nucl. Fusion **55**, 013023 (2015).
  - [2] C. M. Surko, R. E. Slusher, J. J. Schuss, R. R. Parker, I. H. Hutchinson, D. Overskei, and L. S. Scaturro, Phys. Rev. Lett. **43**, 1016 (1979).
  - [3] C. M. Surko and R. E. Slusher, Phys. Rev. Lett. **37**, 1747 (1976).
  - [4] S. Alberti, Nature Physics **3**, 376 (2007).
  - [5] M. Bornatici, R. Cano, O. De Barbieri, and F. Engelmann, Nucl. Fusion **23**, 1153 (1983).
  - [6] R. Prater, Phys. Plasmas **11**, 2349 (2004).
  - [7] G. Gantenbein, H. Zohm, G. Giruzzi, S. Günter, F. Leuterer, M. Maraschek, J. Meskat, Q. Yu, the ASDEX Upgrade Team, and the ECRH-Group AUG, Phys. Rev. Lett. **85**, 1242 (2000).
  - [8] I. G. J. Classen *et al.*, Phys. Rev. Lett. **98**, 035001 (2007).
  - [9] C. Lechte, G. D. Conway, T. Görler, and T. Happel, Plasma Science and Technology **22**, 064006 (2020).
  - [10] A. Snicker, E. Poli, O. Maj, L. Guidi, A. Koehn, H. Weber, G. D. Conway, M. A. Henderson, and G. Saibene, Nucl. Fusion **58**, 016002 (2018).
  - [11] C. Tsironis, A. G. Peeters, H. Isliker, D. Strintzi, I. Chatziantonaki, and L. Vlahos, Phys. Plasmas **16**, 112510 (2009).
  - [12] Y. Peysson, J. Decker, L. Morini, and S. Coda, Plasma Phys. Control. Fusion **53**, 124028 (2011).
  - [13] A. K. Ram, K. Hizanidis, and Y. Kominis, Phys. Plasmas **20**, 056110 (2013).
  - [14] A. K. Ram and K. Hizanidis, Phys. Plasmas **23**, 022504 (2016).
  - [15] E. V. Sysoeva, F. da Silva, E. Z. Gusakov, S. Heuraux, and A. Y. Popov, Nucl. Fusion **55**, 033016 (2015).
  - [16] S. Coda, J. Ahn, R. Albanese, S. Alberti, E. Alessi, S. Allan, H. Anand, G. Anastassiou, Y. Andrébe, C. Angioni, *et al.*, Nucl. Fusion **57**, 102011 (2017).
  - [17] O. Chellaï, S. Alberti, M. Baquero-Ruiz, I. Furno, T. Goodman, B. Labit, O. Maj, P. Ricci, F. Riva, L. Guidi, *et al.*, Plasma Phys. Control. Fusion **61**, 014001 (2018).
  - [18] O. Chellaï, S. Alberti, M. Baquero-Ruiz, I. Furno, T. Goodman, F. Manke, G. Plyushchev, L. Guidi, A. Koehn, O. Maj, *et al.*, Phys. Rev. Lett. **120**, 105001 (2018).
  - [19] F. Riva, C. Tsui, J. Boedo, P. Ricci, and T. Team, Physics of Plasmas **27**, 012301 (2020).
  - [20] F. Jenko, W. Dorland, M. Kotschenreuther, and B. Rogers, Physics of plasmas **7**, 1904 (2000).
  - [21] G. Merlo, S. Brunner, Z. Huang, S. Coda, T. Goerler, L. Villard, A. B. Navarro, J. Dominski, M. Fontana, F. Jenko, *et al.*, Plasma Physics and Controlled Fusion **60**, 034003 (2018).
  - [22] H. Weber, O. Maj, and E. Poli, EPJ Web of Conferences **87**, 01002 (2015).
  - [23] P. Blanchard, Y. Andrebe, H. Arnichand, R. Agnello, S. Antonioni, S. Couturier, J. Decker, T. D. K. DExaerde, B. Duval, I. Furno, *et al.*, Journal of Instrumentation **14**, C10038 (2019).
  - [24] A. Masetto, F. D. Halpern, S. Jolliet, J. Loizu, and P. Ricci, Phys. Plasmas **20**, 092308 (2013).
  - [25] F. D. Halpern, S. Jolliet, J. Loizu, A. Masetto, and P. Ricci, Phys. Plasmas **20**, 052306 (2013).
  - [26] H. M. Mott-Smith and I. Langmuir, Phys. Rev. **28**, 727 (1926).
  - [27] I. Hutchinson, *Principles of plasma diagnostics* (Cambridge University Press, 1987).
  - [28] O. Février, C. Theiler, H. De Oliveira, B. Labit, N. Fedorczak, and A. Baillod, Rev. Sci. Instrum. **89**, 053502 (2018).
  - [29] F. Nespoli, I. Furno, B. Labit, P. Ricci, F. Avino, F. Halpern, F. Musil, and F. Riva, Plasma Phys. Control. Fusion **59**, 055009 (2017).
  - [30] The diagnostic was referred to as *X3TD* in previous publication. The name *O3TD* is more appropriate in this paper since the detection is now performed in ordinary mode.
  - [31] R. A. Fisher, Metron **1**, 3 (1921).
  - [32] O. Chellaï, *Millimeter-Wave Beam Scattering by Edge Turbulence in Magnetically-Confined Plasmas* (EPFL, Lausanne, 2019).
  - [33] C. Tsui, J. Boedo, J. Myra, B. Duval, B. Labit, C. Theiler, N. Vianello, W. Vijvers, H. Reimerdes, S. Coda, *et al.*, Phys. Plasmas **25**, 072506 (2018).
  - [34] I. Furno *et al.*, Phys. Plasmas **15**, 055903 (2008).
  - [35] G. Pereverzev, Physics of Plasmas **5**, 3529 (1998).
  - [36] Y. A. Kravtsov and Y. I. Orlov, goim (1990).
  - [37] *COMSOL RF Module User's Guide v5.2a*.
  - [38] T. Stix, *The Theory of Plasma Waves*, New York: McGraw-Hill (1962).
  - [39] A. Köhn, L. Guidi, E. Holzhauer, O. Maj, E. Poli, A. Snicker, and H. Weber, Plasma Phys. Control. Fusion **60**, 075006 (2018).
  - [40] S. W. McDonald, Phys. Rev. A **43**, 4484 (1991).
  - [41] F. Riva, N. Vianello, M. Spolaore, P. Ricci, R. Cavazzana, L. Marrelli, and S. Spagnolo, Phys. of Plasmas **25**, 022305 (2018).
  - [42] T. Goerler, X. Lapillonne, S. Brunner, T. Dannert, F. Jenko, F. Merz, and D. Told, Journal of Computational Physics **230**, 7053 (2011).

- [43] A. Medvedeva, C. Bottereau, F. Clairet, G. Conway, S. Heuraux, D. Molina, U. Stroth, A. U. Team, *et al.*, in *12th International Reflectometry Workshop (IRW 12)* (2015).
- [44] A. Medvedeva, C. Bottereau, F. Clairet, P. Hennequin, U. Stroth, G. Birkenmeier, M. Cavedon, G. Conway, T. Happel, S. Heuraux, *et al.*, *Plasma Phys. Contr. Fusion* **59**, 125014 (2017).
- [45] O. Maj *et al.*, *Phys. Plasmas*, to be submitted (2021).
- [46] E. Poli, G. V. Pereverzev, and A. G. Peeters, *Physics of Plasmas* **6**, 5 (1999).